

Plastic strain partitioning in dual phase Al₁₃CoCrFeNi high entropy alloy

Wael Abuzaid^{a,*}, Huseyin Sehitoglu^b

^a Department of Mechanical Engineering, American University of Sharjah, PO Box 26666, Sharjah, UAE

^b Department of Mechanical Science and Engineering, University of Illinois at Urbana-Champaign, 1206 W. Green St., Urbana, IL 61801, USA



ARTICLE INFO

Keywords:

High entropy alloys
Dual phase alloy
Plastic strain partitioning
Strain localization
Phase boundaries

ABSTRACT

High entropy alloys present opportunities to develop new materials with unique mechanical properties. Through careful selection of constituent elements and thermal processing, different microstructures with varying properties can be achieved. This study is focused on an interesting class of high entropy alloys with dual phase microstructure, a soft FCC and a hard BCC phase. Specifically, the local material response of Al₁₃CoCrFeNi (atomic %), at the microscale and in the vicinity of phase boundaries, is analyzed using high resolution strain and grain orientation measurements. Different heat treatments resulting in varying phase volume fractions and deformation temperatures were considered. The local response of this high entropy alloy displayed significant heterogeneity in plastic strain accumulation with preferential accumulation in the FCC grains and localizations at phase boundaries. The preferential accumulation of plastic strains in FCC grains (33–85% higher than BCC) was further enhanced with very high temperature heat treatments conducted at 1300 °C. These changes in plastic strain partitioning were associated with the increase in BCC phase volume fraction which was altered during heat treatment. At the macro-scale, the unloading response of Al₁₃CoCrFeNi revealed a nonlinear unloading behavior with large magnitudes of recoverable strains (0.9–1.4%). Deformation at cryogenic temperatures revealed slip dominated plasticity and no changes in the underlying deformation mechanism due to temperate reduction. However, the plastic strain partitioning between the FCC and BCC phases is shown to be affected with larger magnitudes of plastic strains accumulating in the FCC phase, and less in the BCC phase, compared to the room temperature deformation response.

1. Introduction

High entropy alloys (HEA) continue to capture interest in the research community due to their desirable mechanical properties and the potential for further enhancements and tunability through careful selection of constituent elements, composition, and heat treatment [1–4]. Although most studies have been focused on HEAs with single phase compositions, *e.g.*, the FCC FeNiCoCrMn Cantor alloy [5], multi-phase structures are increasingly being explored in the effort to develop new alloys with unique properties [6–8]. In such microstructures, the resulting alloy properties will inherently be dependent on the constituent phases, *e.g.*, their individual strength and ductility [9], the volume fraction of each phase [10,11], and the heterogeneities in deformation introduced by phase boundaries [12]. A proper understanding of the micro-scale response, *i.e.*, at the scale of individual grains and in the vicinity of phase boundaries, is crucial in explaining the macro-scale response and can aid the design and optimization of the alloy properties. This work aims to investigate the local response of a dual phase HEA, particularly the Al₁₃CoCrFeNi (atomic %) system [6,9,13–15].

Through high resolution local strain and grain orientation measurements, we study the dissimilar buildup of plastic strains in the constituent phases and the localizations taking place at phase boundaries. In addition, by subjecting the alloy to different heat treatments, thus altering the volume fraction and composition of the FCC and BCC phases, the changes in the local response due to phase volume fraction variations were also assessed.

The development of dual phase HEAs with one of the phases being soft, to enhance ductility, and a hard second phase, to improve strength, has been the main motivation for recent efforts [1,16]. Changes and deviation from the equiatomic composition present in the widely studied FeMnNiCoCr HEA, has been shown to induce the formation of dual phase structures, FCC and HCP [7]. The introduction of Al, however, has been reported to result in the formation of a ductile FCC and hard BCC phases [6,17–19]. The Al_xCoCrFeNi system has been the subject of many recent studies focusing on the effect of Al concentration on the resulting phase stability [11,15,20], effect of deformation temperature on the mechanical properties and ordering of the BCC and FCC phases [11,21,22], type of processing [23–26], heat treatment effects on

* Corresponding author.

E-mail address: wabuzaid@aus.edu (W. Abuzaid).

microstructure and mechanical properties [10,11,13,27,28], and even studies reporting a rather surprising stress induced martensitic transformation leading to reversible deformation [29]. The aforementioned works have provided valuable insight into microstructural changes, induced by heat treatment and composition changes, and their impact on the macro-scale properties such as hardness and stress-strain response. Ma et al. provide an additional insight into the micro-scale response through the use of *in-situ* Neutron diffraction [29]. By measuring the elastic lattice strains in both phases, they were able to point out a lower yielding behavior in the FCC phase and stress partitioning where the BCC phase was shown to carry higher stresses compared to the FCC phase. There is however less work on plastic strain partitioning between the FCC and the BCC constituent phases. A better understanding of the buildup of plastic strains, locally, and its partitioning between the present phases sheds important and further insight into the micro-mechanical response (e.g., ductility of each phase and the level of mismatch between phases across the phase boundary). This particular aspect will be a subject of investigation in this study and used to explain variations in macro-scale response induced by different heat treatments on Al₁₃CoCrFeNi HEA.

The low temperature performance of some HEAs (i.e., improved toughness, strength, and ductility at cryogenic temperatures) has been one of the most intriguing properties of this class of materials. Several studies have evaluated the low temperature performance of the Al_xCoCrFeNi HEA focusing on the macro-scale mechanical properties and microstructural analysis using the transmission electron microscopy (TEM) [8,21,30]. In general, strength increased with lowering the deformation temperature but, and unlike the equiatomic FeMnNiCoCr system, no improvement in ductility was measured. The reported ductility levels remained consistent across different deformation temperatures which is still valuable given the expected degradation in traditional alloy systems. In the single phase FeNiCoCrMn FCC HEA alloy systems, the activation of deformation twinning at low temperatures has been shown to influence the mechanical response and result in simultaneous enhancements of strength and ductility [3,31–33]. The presence of deformation twins has not been reported for the Al_xCoCrFeNi HEA system which can partially explain the limited ductility. In addition, the presence of the hard BCC phase could be the ductility limiting factor and not the details of the deformation mechanisms, slip or twinning, in the soft FCC phase [9,10]. In this work, we aim to provide further insight into the *micro-scale* material response of Al₁₃CoCrFeNi (atomic %) at cryogenic temperatures. Particularly we focus on, evaluating the active deformation mechanisms in the FCC phase and whether deformation twinning contributes to the built up of plastic strains. In addition, we quantitatively evaluate strain partitioning between the soft FCC and hard BCC phases in an attempt to determine if the buildup of mismatch between these two constituent phases influences the resultant alloy ductility.

High resolution local strain measurements combined with electron backscattering diffraction (EBSD) has been shown to provide effective means to evaluate the local deformation response including the activation of slip [34–36], twinning [37], and the local built up of strains at with sub-grain level resolution [34]. These techniques will be utilized in this work to shed valuable insight into the micro-scale response of the Al₁₃CoCrFeNi (atomic %) HEA. We focus on quantifying the plastic strain partitioning between the constituent phases and the localizations of strains in the vicinity of phase boundaries for different phase volume fractions and deformation temperatures.

2. Materials and methods

An ingot of FeNiCoCrAl₁₃ (atomic %) was grown using the Bridgman technique in an argon atmosphere. Homogenization of the crystal was conducted in a helium atmosphere at 1100 °C for 24 h followed by quenching in water. The resulting microstructure was a dual phase material with FCC (Fe and Cr rich) and BCC (Ni and Al rich)

phases. The BCC phase had a single < 001 > orientation while the FCC grains were either of a < 001 > or < 110 > grain orientations (relative to the loading axis). Crystal orientations were determined using Electron backscatter diffraction (EBSD) and compositions using EDX. Dogbone tension samples with 3 × 1.5 mm gauge section and 8 mm gauge length were electric discharge machined from the ingot. Samples tested in this condition are referred to “As Grown” samples throughout the manuscript. Heat treatment, for selected samples, was conducted in air at two different temperatures, 1100 °C for 90 min and 1300 °C for 60 and 120 min. In all cases, the heat treatments were terminated by quenching the samples in water. All samples were polished using SiC paper to prepare the surface for high resolution *ex-situ* DIC measurements following the procedure detailed in [38].

Two different types of experiments were carried out in this work; *in-situ* DIC where loading was carried out in a micro-loading stage and *ex-situ* DIC with deformation carried out in a standard load frame with postmortem *ex-situ* strain measurements of the residual deformation. For the *in-situ* type experiment, DIC reference and deformed images were collected using an optical microscope equipped with a micro-loading stage (20× magnification with imaging resolution of 0.22 μm/pixel). For samples dedicated for high resolution residual strain measurements (i.e., *ex-situ* type experiments), DIC reference and deformed images were captured using optical microscopy at either 25 or 50× magnifications (corresponding to 0.17 and 0.09 μm/pixel, respectively). Loading was conducted using an Instron servo hydraulic load frame, in strain control with an average strain rate of 1^{−3} s^{−1}, to 3% total normal strain and then unloaded in load control. After deformation, samples were removed from the load frame to capture deformed images of the region of interest (outlined with fiducial markers prior to loading).

3. Results and analysis

Optical images showing the morphology of “As Grown” and heat treated samples are shown in Fig. 1. As confirmed through EBSD, the microstructure had two distinct phases, an FCC (Fe and Cr rich) and BCC (Ni and Al rich) phases (shown in Fig. 1a). Aging heat treatments up to four hours at temperatures below 900 °C did not cause any noticeable difference in either the volume fraction or composition of the phases compared to the “As Grown” conditions. However, heat treatments conducted at 1100 °C did alter the relative distribution of phases as shown in Fig. 1b. More noticeable changes were observed at 1300 °C heat treatments as shown in Fig. 1c-d. An obvious increase in the size of the FCC and BCC regions was clearly observed. In addition, the volume fraction of the BCC phase has changed and increased, for example, from 25% for the “As Grown” conditions to 51% after a 120 min heat treatment at 1300 °C. The composition of the corresponding phases has also changed during heat treatment, an example is shown in Fig. 1e.

As noted above, heat treatments conducted at high temperatures resulted in clear microstructural changes and lead to an increase in the BCC phase volume fraction and alteration in both FCC and BCC phase compositions. To assess the impact of these changes on the macro-scale response, samples were loaded to 3% total strain, in tension, and unloaded in load control. The stress-strain response for the “As Grown” sample and a selected heat treated sample are shown in Fig. 2a. The heat treated samples, in all cases, displayed a steep hardening response, beyond yielding and up to ~ 1.5% total strain, compared to the “As Grown” conditions [$\Delta\sigma_{\text{heat treated } 1300^{\circ}\text{C for } 120 \text{ min}} \cong 290\text{MPa}$ compared to $\Delta\sigma_{\text{As Grown}} \cong 160\text{MPa}$]. Upon unloading, all samples displayed a rather large recovery response with measured recoverable strain ranging from 0.9% for the “As Grown” conditions to a remarkable 1.4% for samples heat treated at 1300 °C. A summary of the macro-scale measured properties is shown in Fig. 2b. An increase in the amount of recoverable strain is clearly observed after 1300 °C heat treatments. This suggests a correlation between the phase volume fraction (shown in change in Fig. 1) and the measured recoverable strain. This topic is subjected to further discussion in Section 4.

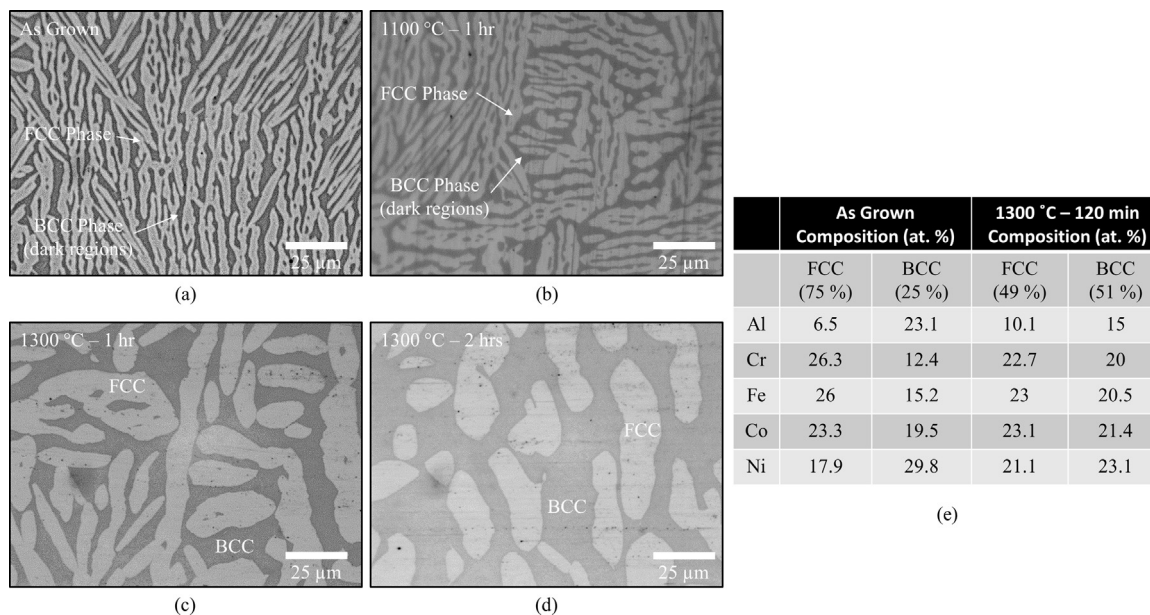
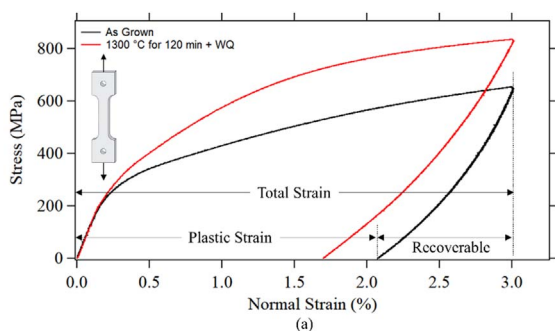


Fig. 1. (a) Optical image showing the microstructure of the dual phase “As Grown” HEA. (b) – (c) optical images showing the changes in structure after different heat treatments. (e) A summary of phase volume fractions, obtained from EBSD, and composition of individual phases (EDX) for two different heat treatments.



Heat Treatment	Modulus E (GPa)	Yield Strength (0.2 % offset) (MPa)	Total Strain (%)	Plastic Strain (%)	Recoverable Strain (%)
As Grown	138	330 MPa	3.0	2.1	0.9
1100 °C – 90 min	140	370 MPa	3.0	2.2	0.8
1300 °C – 60 min	142	410 MPa	3.0	1.6	1.4
1300 °C – 120 min	136	385 MPa	3.0	1.7	1.3

(b)

Fig. 2. (a) Stress-strain response of selected samples loaded in tension at room temperature. (b) A summary of the macro-scale properties measured after different heat treatments. A rather large recoverable strain component was measured for all samples.

To better understand the micro-scale response, a sample in the “As Grown” conditions was loaded in tension using a micro-loading stage fitted on an optical microscope. During loading, deformed images were captured *in-situ* at $20\times$ magnification ($0.22\ \mu\text{m}/\text{pixel}$) for DIC strain measurements. The stresses were calculated using the load measured from the micro-loading stage force transducer while the strains were calculated by averaging the normal strain field (*i.e.*, along the loading direction which is designated as $[100]$ direction in sample frame) in a $250 \times 250\ \mu\text{m}$ region on the sample’s surface. The resulting stress-strain response is shown in Fig. 3a. Fig. 3b shows an optical image of the region of interest which was outlined using micro-hardness fiducial markers. These markers were crucial for subsequent alignment of the DIC strain field with the underlying microstructure. EBSD analysis in the region of interest prior to loading revealed an approximately $\langle 001 \rangle$ and $\langle 110 \rangle$ grain orientations for the FCC phase and predominantly $\langle 001 \rangle$ for the BCC phase as shown in the inverse pole figures (IPF) presented in Fig. 3c.

The buildup of local strains with continued loading can be observed from DIC strain contour plots as shown, for example, at three different stress levels in Fig. 3d-f (points A, C, and D in Fig. 3a). The phase boundaries were overlaid on each of the contour plots using a MATLAB code which was written to extract the location of FCC and BCC phases using the optical image contrast (Fig. 3b). The fiducial markers, which were visible in both the optical image of the microstructure and the DIC images, were used to transform the location of the phase boundaries to the DIC contour plots. In addition, as each grain in the region of interest can be unambiguously described as either an FCC or BCC grain based on image contrast, the data overlay procedure provided accurate description of the phase for each point in the DIC region. Therefore, the buildup of deformation in these two different phases can be quantified and analyzed separately. A summary of the total average strain (both FCC and BCC), the FCC average strains, and the BCC average strains are shown in Table 1 for the four points marked in Fig. 3a (*i.e.*, points A – D). Given the size of the BCC and FCC grains, the volume fraction of the BCC phase ($\sim 25\%$), and the resolution of the DIC measurements, no noticeable difference between the response in the FCC and BCC grains was observed as summarized in Table 1. The strain field standard deviation quantifies the heterogeneity in deformation which was shown to increase at higher levels of deformation (*e.g.*, increasing from 0.19% at point A to 1.02% at C prior to unloading). Again, no noticeable difference between the FCC and BCC phase response was measured for the sample discussed in Fig. 3 (*i.e.*, “As Grown” conditions and room temperature deformation).

As shown earlier in Figs. 1 and 2, heat treatment had a significant effect on the BCC/FCC grain sizes and volume fractions. Samples subjected to the $1300\ \text{°C}$ heat treatments for 60 and 120 min resulted in the most noticeable changes in terms of grain size and phase volume fraction. Therefore, to further understand the impact of these microstructural changes on the mechanical properties, compared to the “As Grown” conditions, we subject the heat treated samples to identical 3% deformation, in tension, followed by unloading. High resolution DIC strain measurements were collected from the deformed samples after unloading (*i.e.*, *ex-situ* residual deformation measurements). Reference and deformed images were collected using an optical microscope at $50\times$ magnification ($0.09\ \mu\text{m}/\text{pixel}$). A total of 6 images were captured to cover a $250 \times 250\ \mu\text{m}$ region of interest following the procedure presented in [34,39]. The microstructural information (*i.e.*, grain size

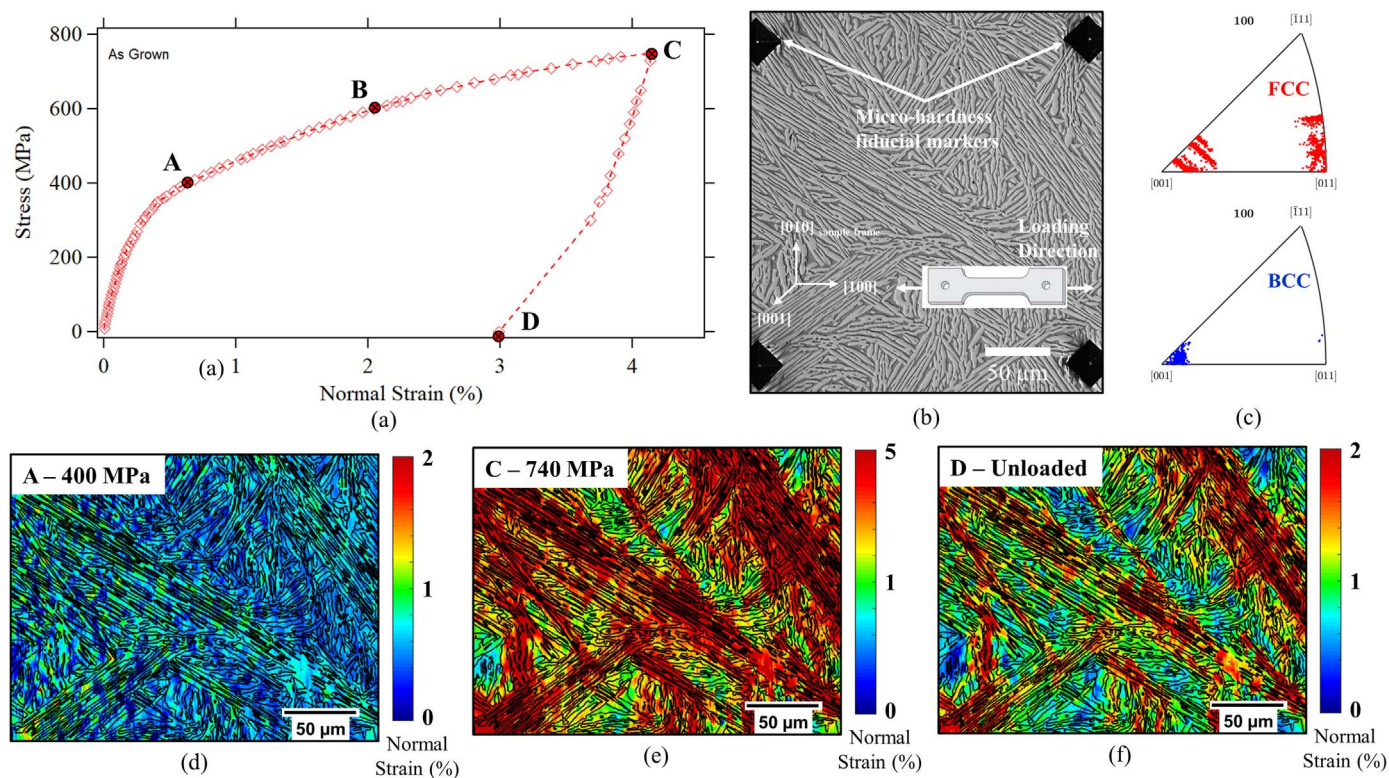


Fig. 3. (a) Stress-strain response of “As Grown” sample loaded in tension using micro-loading stage. (b) Optical image showing the microstructure in the region of interest on the sample’s surface (DIC region). (c) IPFs showing the grain orientations for the FCC and BCC phases. (d) – (f) DIC strain contour plots of the normal strain with overlaid phase boundaries at different stress levels.

and phase) were available from optical images after surface polishing and prior to the application of the DIC speckle pattern.

Fig. 4a shows a comparison between the stress strain response of a sample subjected to 60 min heat treatment at 1300 °C and a sample in the “As Grown” conditions. A significant increase in strength, strain hardening rate, and recoverable strains can be clearly observed in the macro-scale measurements. An optical image showing the microstructure in the region of interest (prior to deformation) is shown in Fig. 4b. The high resolution DIC strain measurements after unloading are shown in Fig. 4c-d for the same region of interest marked in Fig. 4b. By separating the DIC strains into FCC and BCC (using the underlying microstructure and a MATLAB code as explained above), a dissimilar accumulation of residual plastic strains is revealed (Plastic strain partitioning). As shown in Fig. 4c, the average strain in the FCC grains was ~ 1.8% compared to 1.3% in the BCC grains (*i.e.*, FCC plastic strain 38% higher than BCC). Also the standard deviation, which is a measure of deformation heterogeneity, was also higher for the FCC grains, which is expected given the higher level of plastic deformation. Such a variation between the residual deformation in the FCC and BCC phases was not detected from samples in the “As Grown” conditions (see Fig. 3 and Table 1) which suggests that the phase volume fraction and grain size must have induced this behavior. The full field strain contour plot shown in Fig. 4d reveals high levels of residual strains in FCC grains

compared to BCC regions, which is consistent with the summary data presented in Fig. 4c. In addition to the preferential accumulation of plastic strains in selected FCC grains, phase boundaries were shown to have localized deformation in their vicinity as marked for multiple boundaries in Fig. 4d with black and white arrows. Various factors can induce such a response, *e.g.*, the incompatibility across the interface and the formation of dislocation pileups, as will be discussed in Section 4.

With heat treatment time increased from 60 min (presented in Fig. 4) to 120 min, a similar increase in strength and amount of recoverable strain was observed as shown in Fig. 5a. DIC analysis of plastic strain partitioning between the FCC and BCC phases for the microstructure shown in Fig. 5b is presented in Fig. 5c. A noticeable increase in the average strain accumulation in the FCC phase was observed (2.36%) compared to the 60 min heat treatment case (1.78%). The BCC phase average strain did not experience a significant change (average 1.34% for the 60 min heat treatment compared to 1.27 for the 120 min treatment). The reduction in the FCC volume fraction with longer heat treatments, and assuming no changes in the ductility of the constituent phases, can explain such a response. As the FCC regions have to accommodate the same amount of total plastic strain in a smaller region, the FCC grains have to deform more and accumulate higher levels of plastic strains. The full field strain contour plot shown in Fig. 5d confirms the preferential accumulation of plastic strains in

Table 1

Summary of the normal strain field properties – As Grown conditions.

Point (Stress)	Average Normal Strain (%)	FCC Average Normal Strain (%)	BCC Average Normal Strain (%)	Normal Strain Stdv. (%)	FCC Normal Strain Stdv. (%)	BCC Normal Strain Stdv. (%)
A (400 MPa)	0.62	0.63	0.62	0.19	0.19	0.19
B (600 MPa)	2.04	2.06	2.03	0.46	0.46	0.46
C (740 MPa)	3.94	3.97	3.90	1.02	1.02	1.02
D (Unloaded)	3.02	3.05	2.98	1.00	1.00	0.99

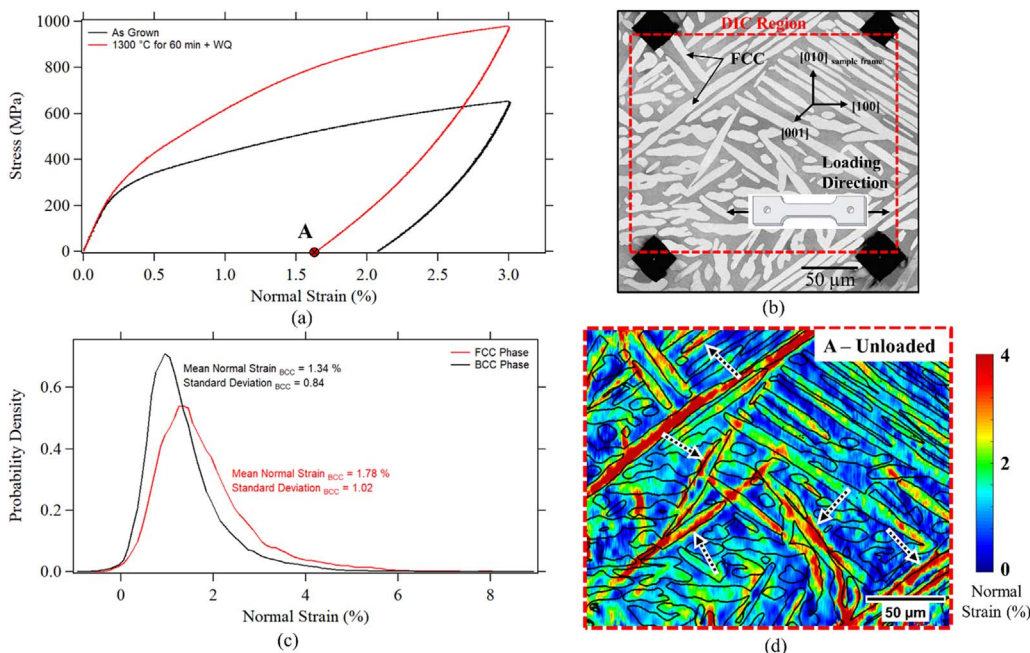


Fig. 4. (a) Comparison between the stress-strain response of “As Grown” and heat treated sample for 60 min at 1300 °C. (b) Optical image showing the microstructure in the region of interest on the sample’s surface (DIC region). (c) Strain histograms of the normal strain (along loading direction) for the FCC and BCC regions. (d) DIC strain contour plots of the normal strain with overlaid phase boundaries. Black and white arrows point to localizations at phase boundaries.

FCC grains. Localizations in the vicinity of phase boundaries was also very evident in this case as pointed with black and white arrows on the contour plot. In addition, strain accumulations, locally, and extending between adjacent FCC grains, thus passing through BCC regions, has been observed in multiple locations as pointed with red and white arrows on the strain contour plot. These features can be the result of slip transmission across the phase boundaries between the soft FCC grains, through the hard BCC phase.

A summary of the plastic strain partitioning results for the different treatments is provided in Table 2. The volume fractions were estimated from the optical images of the microstructure (Fig. 3b, Fig. 4b, and Fig. 5b). As discussed above, the increase in the BCC volume fraction, and the associated decrease in the FCC volume fraction, has led to an increase in the average FCC strains. In addition, and as pointed out from the strain field standard deviation, an increased level of deformation heterogeneity was also observed. The higher levels of plastic strains in

the FCC regions will inherently result in higher levels of heterogeneity which is confirmed by the results presented in Table 2. We also notice a pronounced increase in the BCC strains standard deviation (*i.e.*, becoming more heterogeneous), the transmission of slip between the FCC soft grains through the BCC regions can partially explain this result. It is noted that for the 60 min heat treatment, higher FCC volume fraction compared to the 120 min heat treatment, the localization of strains was more pronounced within the larger FCC grains with less extension or transmission across the BCC phase. The BCC strain field standard deviation was less in this case compared to the 120 min heat treatment case were the full field contour plots pointed to multiple locations with possible slip transmission across the BCC regions.

Another topic of interest in this work is the micro-scale response of Al₁₃CoCrFeNi HEA at low temperatures. Fig. 6a presents a comparison between the stress-strain response for three samples deformed at room temperature (RT), - 25 °C, and - 196 °C. Cooling was achieved

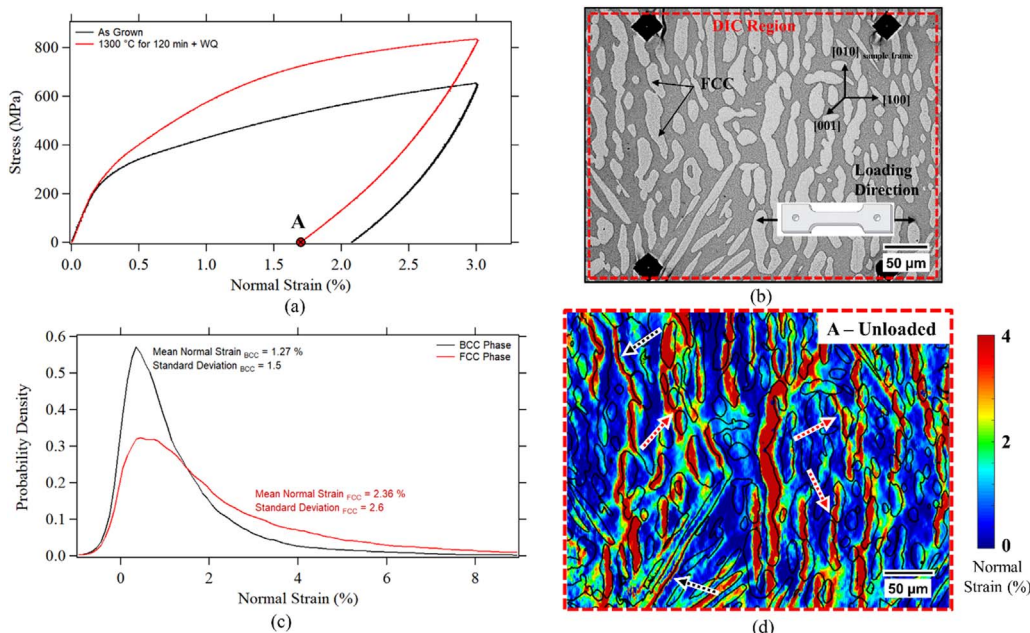


Fig. 5. (a) Comparison between the stress-strain response of “As Grown” and heat treated sample for 120 min at 1300 °C. (b) Optical image showing the microstructure in the region of interest on the sample’s surface (DIC region). (c) Strain histograms of the normal strain (along loading direction) for the FCC and BCC regions. (d) DIC strain contour plots of the normal strain with overlaid phase boundaries. Black and white arrows point to localizations at phase boundaries. Red and white arrows point to localizations extending between FCC grains through BCC regions indicating possible slip transmission across the phase boundaries.

Table 2

Summary of the plastic strain partitioning for different heat treatments.

Heat Treatment	BCC Volume Fraction Estimate	Residual Normal Strain (%)	FCC Average Normal Strain (%)	BCC Average Normal Strain (%)	Normal Strain Stdv. (%)	FCC Normal Strain Stdv. (%)	BCC Normal Strain Stdv. (%)
As Grown	39% (Fig. 3b)	3.02	3.05	2.99	1.00	1.00	0.99
1300 °C – 60 min	46% (Fig. 4b)	1.58	1.78	1.34	0.97	1.02	0.84
1300 °C – 120 min	57% (Fig. 5b)	1.73	2.36	1.27	2.14	2.60	1.50

through custom load frame grips which allowed for liquid nitrogen (LN) circulation. The sample's temperature was measured using a thermocouple fitted on the back surface. Isothermal conditions were achieved and maintained for 5 min prior to deformation. The strength increased by lowering the temperature, however the strain hardening rate was almost identical for the temperatures considered. The activation of twinning at LN temperatures for the FeNiCoCrMn is accompanied by pronounced increase in the hardening rate compared to slip dominated deformation. The absence of such response for the $\text{Al}_{13}\text{CoCrFeNi}$ suggests that no major change in the underlying deformation mechanism is expected between samples deformed at RT and LN temperatures.

To shed further insight into the local deformation mechanism at LN temperatures, EBSD data was collected from a $250 \times 250 \mu\text{m}$ region of interest before deformation and after applying 3% normal strain, in tension, and unloading at -196°C (LN). Micro hardness fiducial markers were used to outline the region of interest so EBSD data can be collected from the same region on the sample's surface. Figs. 6b and c shows the grain orientation and the phase map, respectively, after deformation (*i.e.*, $\sim 2\%$ residual strain). Figs. 6d and e shows the IPF plots for both phases prior to and after loading (obtained from the same sample and region of interest). As the grain orientation data before and after deformation were very similar, this points to slip dominated activity with no sign of activation of deformation twinning in the FCC phase.

High resolution and full field strain measurements at the micro-scale were also conducted for samples deformed at LN temperatures. To achieve very

high resolutions, reference images were collected in the scanning electron microscope (SEM) at three different magnification; $1000 \times$ ($0.062 \mu\text{m}/\text{pixel}$), $3000 \times$ ($0.031 \mu\text{m}/\text{pixel}$), and $4000 \times$ ($0.023 \mu\text{m}/\text{pixel}$). The reference images were captured after EBSD data collection with no stage tilting. Deformed images were captured under the same condition after deformation at -196°C . The reference images taken at the three different magnifications are shown in Fig. 7a-c. Only a single SEM image was captured at each magnification which results in a reduction in the field of view (*i.e.*, the region of interest) with magnification increase as shown in Fig. 7a. Nevertheless, the DIC measurement resolution improve significantly which allows more detailed analysis of the localization of plastic strains in the vicinity of phase boundaries and a more accurate assessment of the strain partitioning between the constituent phases. The full field normal strain contour plots are shown in Fig. 7d-f for the three considered magnifications. The results point to a preferential accumulation of plastic strains in FCC grains as depicted visually from the contour plots and summarized quantitatively in Table 3. Notice that as the resolution improves with increasing magnification, the difference between the accumulation of residual strains in the two phases become clear and more pronounced. We note that such a response, although observed for the heat treated samples, was not detected for the “As Grown” conditions when deformation was conducted at RT. This quantitatively points to higher levels of mismatch between the constituent phases at lower deformation temperatures.

To unambiguously determine the underlying deformation mechanism for the $\text{Al}_{13}\text{CoCrFeNi}$ HEA when subjected to cryogenic temperature deformation, high magnification SEM micrographs and EBSD

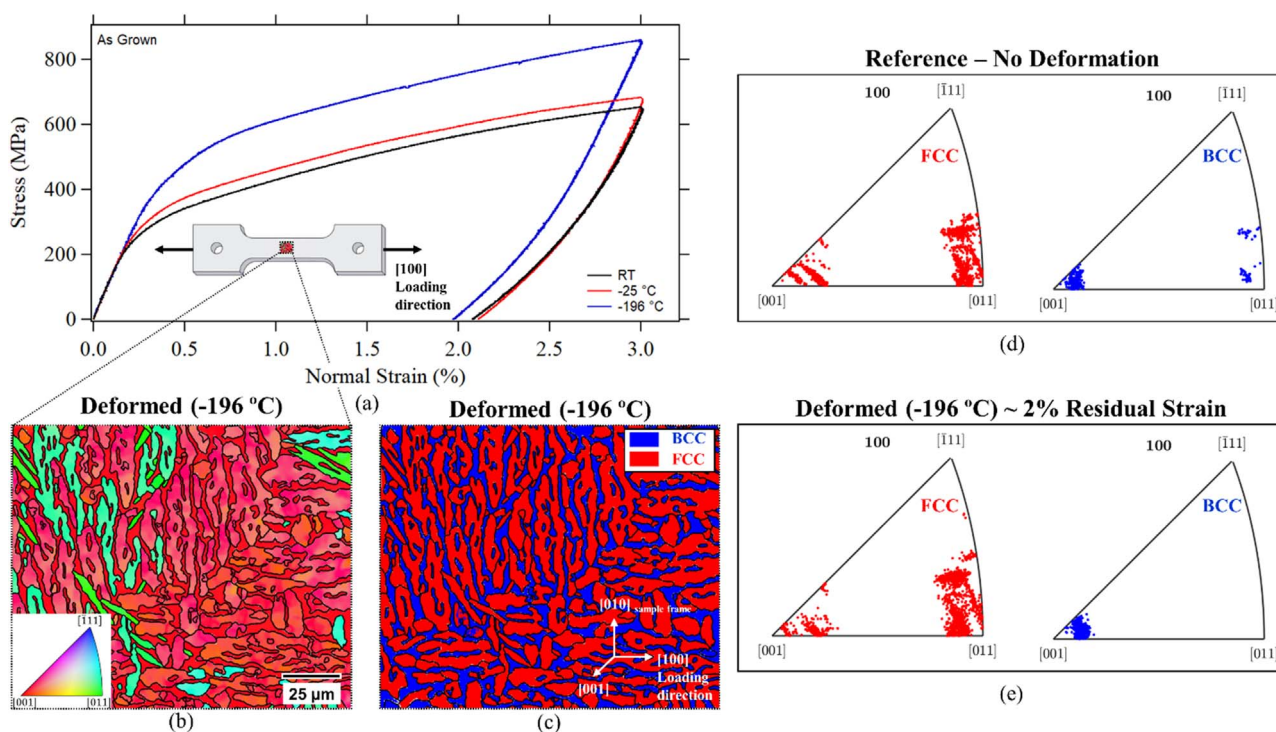


Fig. 6. (a) Comparison between the stress-strain response at RT, -25°C and -196°C . (b) – (c) Grain orientation map and phase map, respectively, obtained after deformation for the sample loaded at -196°C as shown in (a). (d) IPFs for the FCC and BCC phases in the region of interest shown in (b). Data collected prior to loading. (e) Same as (d) but after loading.

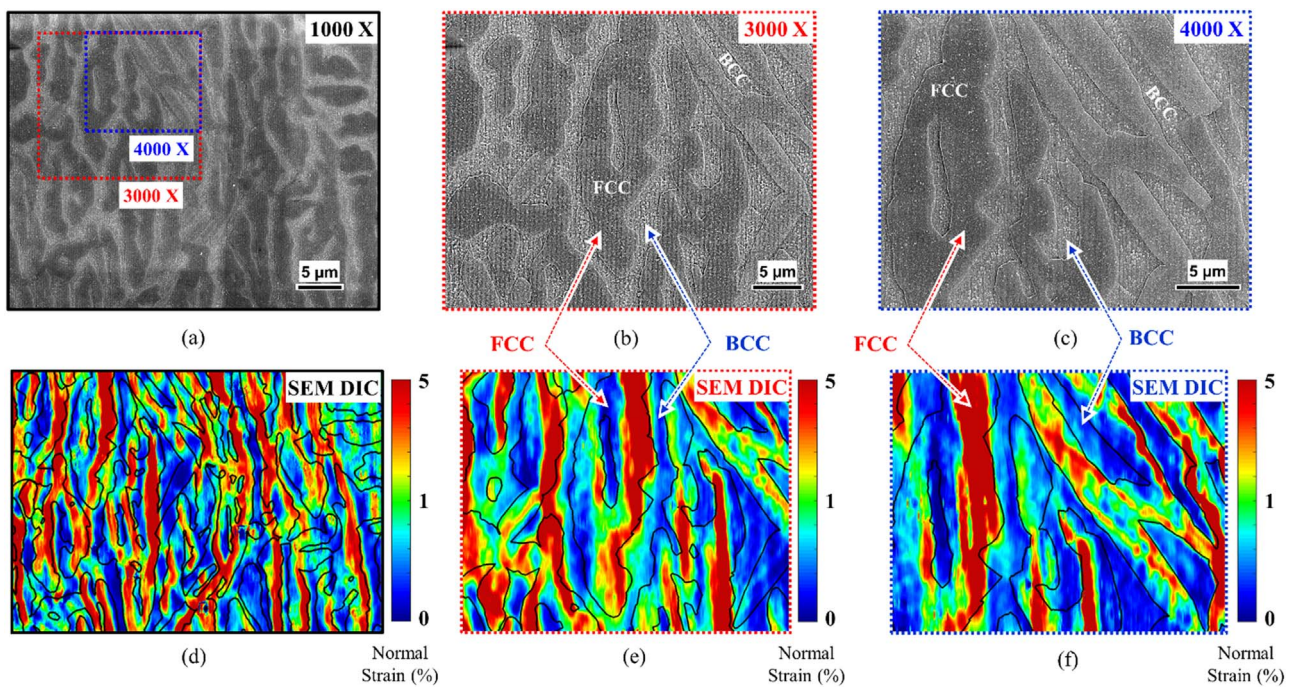


Fig. 7. (a)–(c) DIC reference images captured using the SEM at three different magnifications. The area outlined with a red and blue rectangles in (a) represents the regions of interest at 3000 × and 4000 × magnifications shown in (b) and (c), respectively. (d)–(f) Full field strain contour showing the normal strain after deformation at $-196\text{ }^{\circ}\text{C}$ loading temperature. See Table 3 for data summary.

data were collected on a sample deformed at $-196\text{ }^{\circ}\text{C}$. Fig. 8a shows a high magnification SEM image of a deformed sample showing two FCC grains, marked as Grain 1 and Grain 2, and BCC regions. The two selected grains have roughly a $\langle 001 \rangle$ and $\langle 110 \rangle$ orientations relative to the loading direction which is representative of the entire microstructure. A Grain orientation map and a phase map for the same region in Fig. 8a are presented in Fig. 8b–c, respectively. The EBSD data within the two FCC grains does not point to any twinning activity, which would cause a 60° misorientation across the twin boundary. Therefore, the plastic deformation within the FCC soft grains is dominated by slip at the strain levels considered in this work. This is further confirmed by conducting slip trace analysis on the SEM image in Fig. 8a. Using the grain orientation data collected from EBSD, the crystallographic planes associated with the slip traces on the sample's surface were determined (*i.e.*, described as one of the $\{111\}$ slip planes). By calculating the Schmid factor for each of the possible twelve FCC slip systems, the systems with obvious slip trace on the sample's surface and having the highest Schmid factor were considered to be activated. Based on this analysis, the activated slip in both of the representative FCC grains was determined to take place on the systems with highest Schmid factors as marked for both grains in Fig. 8a (Schmid behavior). This further confirms slip dominated deformation under the strain levels and temperatures considered in this study.

4. Discussion

Previous works on the $\text{Al}_x\text{CoCrFeNi}$ HEA system have pointed to a strong

structure dependence based on the Al concentration [6,9,17–19,24]. Given the considered alloy composition (*i.e.*, $\text{Al}_{13}\text{CoCrFeNi}$ which corresponds to ~ 0.6 mol fraction), a dual phase microstructure was expected, which is consistent with the results presented in this work. It should be pointed out, however, that a wide variation of microstructures has in general been reported in the literature for similar compositions. The difference in processing routes and the subsequent thermal treatments along with the limited understanding of phase stability in this alloy contributes to the reported variability [19]. The samples considered in this experimental study were homogenized as described above resulting in relatively stable properties. Aging treatments at temperatures $< 900\text{ }^{\circ}\text{C}$ caused no noticeable changes in microstructure. However, once the heat treatment temperature was increased to $1300\text{ }^{\circ}\text{C}$, which based on the calculated phase maps reported in [19] would place the alloy in a dual phase region slightly below the expected $\sim 1350\text{ }^{\circ}\text{C}$ melting temperature, significant changes in the microstructure were introduced. An increase in the BCC volume fraction along with coarsening in the FCC grains and a departure from their original lamella structure present in the “As Grown” conditions was observed. In addition, phase composition changes were measured for both of the constituent phases. These changes did alter the mechanical properties at the macro-scale as summarized in Fig. 2 (*e.g.*, strength) as well as the micro-scale as reported in Table 1 (*e.g.*, plastic strain partitioning between phases). Understanding the impact on the mechanical properties, particularly at the micro-scale, was the focus in this work. However, it's important to note that further work is needed to develop a better understanding of phase stability and thermal processing of the $\text{Al}_x\text{CoCrFeNi}$ HEA system as they have a major impact on the eventual alloy strength and ductility as shown in this study.

Table 3
Summary of the plastic strain partitioning for cryogenic temperature deformation ($-196\text{ }^{\circ}\text{C}$).

Magnification	Region of Interest (μm^2)	Residual Normal Strain (%)	FCC Average Normal Strain (%)	BCC Average Normal Strain (%)	Normal Strain Stdv. (%)	FCC Normal Strain Stdv. (%)	BCC Normal Strain Stdv. (%)
1000 ×	4800	1.68	1.91	1.26	1.08	1.11	0.86
3000 ×	1200	1.75	2.06	1.20	1.30	1.41	0.84
4000 ×	660	1.62	2.05	0.81	1.48	1.61	0.69

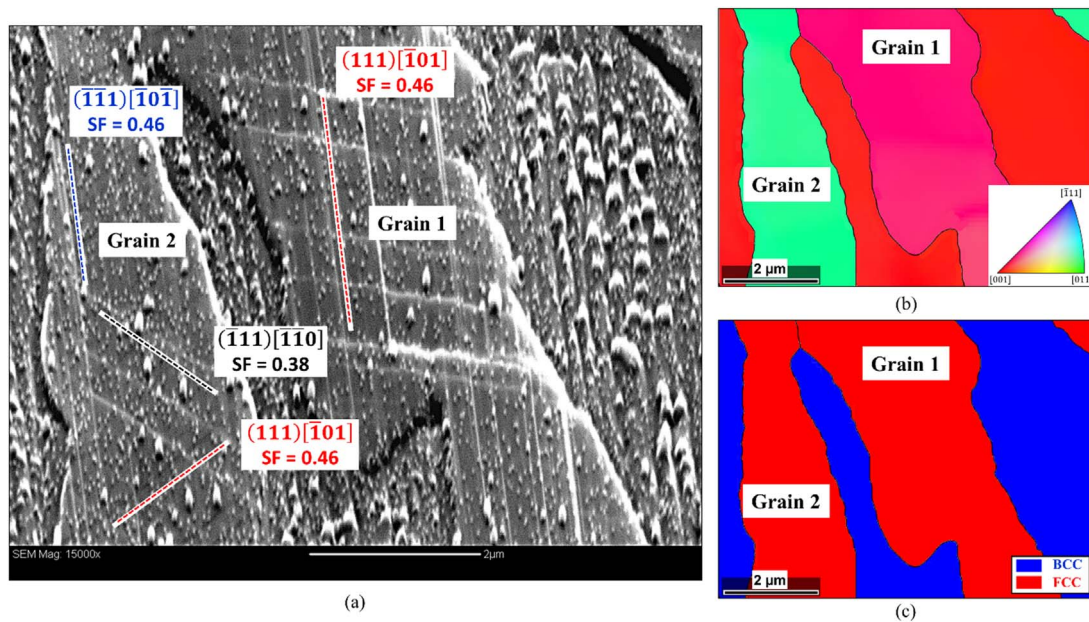


Fig. 8. (a) SEM image of a selected region following 3% deformation at cryogenic temperature ($-196\text{ }^{\circ}\text{C}$). The activated slip system and their corresponding Schmid factors are marked for the FCC grains. (b) – (c) Grain orientation and phase maps for the same region shown in (a), respectively.

A proper analysis of properties at the micro-scale is crucial in understanding the inhomogeneity of deformation at small length scales (sub-grain and in the vicinity of interface boundaries). The resulting strain localizations at such levels effects the material strength, ductility levels and is a precursor to damage initiation [9,10]. The full field strain measurements conducted on “As Grown” samples and heat treated samples in this work revealed a difference in the local material response as manifested by changes in the plastic strain partitioning between the FCC and BCC constituent phases. The average strain in the FCC phase increased with the introduction of a $1300\text{ }^{\circ}\text{C}$ heat treatment and further increased with additional treatment time. These changes are most probably related/induced by the increase in the BCC volume fraction and coarsening in the FCC grains. The BCC phase is known to be a harder phase compared to FCC, consequently, and as the BCC phase volume fraction increases with heat treatment, the FCC phase has to deform more in order to accommodate the same levels of deformation. This results in higher magnitudes of strain accumulation in the FCC phase with BCC volume fraction increase. The relatively unchanged BCC average strain for the two heat-treated samples presented in Table 2 further confirms this conclusion (i.e., although BCC volume fraction increased, the average BCC strain did not, FCC phase had to accommodate more strain). In addition, the associated FCC grain size increase will inherently make the movement of slip dislocation easier over longer distances compared to smaller grains where impedance to their motion is expected from interface boundaries.

As discussed above, heat treatments leading to FCC grain size increase and reduction of its originally closely spaced lamella structure resulted in higher levels of strain accumulation in the FCC phase. On the macro-scale, and despite the reduction in the number of interface boundaries which would act as obstacles for dislocation motion and enhance the strength, the alloy strength increased. The strengthening in this case is most probably associated with the presence the hard BCC phase. The stress partitioning during loading is expected to favor more the harder BCC phase [29], thus leading to higher stresses at similar levels of deformation. The second phase (hard BCC) strengthening has obviously surpassed the reduction in strength expected due to FCC grain coarsening. Since the two strengthening mechanisms are altered differently during heat treatment, the observed trend is not expected to be linear and eventually the strength should start to drop with further FCC grain size increase. This suggests that the alloy strength can be

optimized through a careful selection of the heat treatment time. For the heat treatments conducted in this work at $1300\text{ }^{\circ}\text{C}$, the 120 min treatment experienced a slight drop in strength compared to the 60 min treatment (compare stress-strain curves shown in Figs. 4a and 5a.). Based on the previous discussion, this indicates that the optimal heat treatment time at this temperature has to be between 60 and 120 min.

The unloading behavior of the $\text{Al}_x\text{CoCrFeNi}$ HEA was characterized by a non-linear unloading curve and large recoverable strains. The deviation from linear elastic recovery can be induced by various aspects. Although Ma et al. have reported a stress induced martensite transformation for this alloy [29], it is unlikely that the behavior observed in this work is due to the superelastic response present in shape memory alloys. The EBSD data collected after unloading does not point to any residual martensite in the deformed samples. The response, however, is comparable to non-linear recovery reported for some high strength dual phase steels but with the recovery strains being considerably higher. Various theories have been proposed to explain the rather large amounts of recoverable strains. These include the presence of residual stresses, reverse yielding in the soft ferrite phase, the repelling of dislocation in pileups following load release, and the bowing of dislocation lines during unloading [40–45]. The *in-situ* high resolution local strain measurements presented in Fig. 3 do not clearly point to any reversed yielding mechanism. The strain contour plot in Fig. 3e just before unloading and Fig. 3f after unloading points to local reduction in the strains but no additional accumulation, which would be induced in the case of reversed yielding, during unloading. The large volume fraction of the hard BCC phase and the development of internal stresses due to incompatibility around the phase boundaries are more likely to influence the observed non-linear unloading response. As shown in the summary presented in Fig. 2b, the heat treatments which caused a change in the BCC volume fraction were accompanied by an increase in recovery strains after loading to similar deformation levels. The relaxation taking place at dislocation pileups can also explain the large strain recovery. The strain localizations at phase boundaries similar to what is shown in Fig. 5d are induced by slip in the FCC grains and the formation of pileup at the FCC/BCC boundary. As these dislocations are hard to transmit through the phase boundary to the BCC regions (as confirmed by the preferential accumulation of strains in the FCC grains), high local stresses will develop. Relaxation taking place in the vicinity of these highly stressed regions once loading is removed

will contribute to the relatively large recoverable strains reported for this alloy.

Studies on the low temperature response of the $\text{Al}_x\text{CoCrFeNi}$ HEA system remains limited [21,30]. The EBSD and high resolution strain measurements conducted in this work (Figs. 7 and 8) supports the previous observations of slip dominated deformation even at cryogenic temperatures. Compared to RT deformation, although slip dominates in both cases, the mismatch between the two consistent phases was more pronounced with higher level of plastic strains accumulation in the FCC grains relative to the hard BCC phase. This partitioning in plastic strains, which is indicative of the mismatch and incompatibility at the grain level, was not observed for RT deformation in “As Grown” samples. The buildup of strains preferentially in the FCC phase is accompanied by the creation of pileups impinging at phase boundaries. As discussed above, this results in higher stress levels and can be the source of the large recoverable strains upon unloading. The slight increase in recovery strains as shown in Fig. 6a, compared to RT deformation (both same heat treatment), is consistent with the observation of higher levels of strain accumulation in the FCC phase. It still remains unclear, however, why did the BCC phase accumulate less strains at -196°C compared to RT deformation. Changes in ductility and strain hardening properties of the BCC phase can be expected at lower temperatures and can potentially result in such changes. In addition, the accumulation of slip in the BCC phase can also be hindered by the phase boundary properties and its tendency to allow transmission of slip dislocations from the softer FCC phase. Studies focused on identifying the degradation in ductility and any changes in the slip transmission properties at low temperature can shed further insight into this observed response.

5. Conclusions

The work supports the following conclusions:

1. The $\text{Al}_x\text{CoCrFeNi}$ HEA alloy is characterized by a heterogeneous local deformation response and dissimilar plastic strain accumulation among the FCC and BCC constituent phases.
2. Aging heat treatments at temperatures up to 800°C produced insignificant changes to the microstructure of the alloy. However, very high thermal treatments conducted at 1300°C caused pronounced changes to the phase volume fractions and the morphology of the microstructure. With longer heat treatment, the FCC grain size increased and deviated from the originally fine lamella structure.
3. The amount of plastic strain partitioning was shown to depend on phase volume fraction and FCC grain size. Increasing the BCC phase volume fraction through heat treatment resulted in higher levels of plastic strain accumulation in the larger FCC grains compared to the BCC phase.
4. Strain localizations at phase boundaries were observed through high resolution strain measurements. These localizations were associated with the formation of pileups at the interface boundary.
5. The unloading response of the HEA was non-linear with rather large magnitudes of recoverable strains.
6. Deformation at cryogenic temperatures revealed no changes in the underlying deformation mechanism due to temperate reduction; the plasticity was still accommodated by slip activity. Compared to RT deformation, larger magnitudes of plastic strains were shown to accumulate in the FCC phase and less in the BCC phase with temperature reduction.

Acknowledgements

This research was supported by National Science Foundation grant NSF CMMI-1562288, which is gratefully acknowledged. The corresponding author would like to acknowledge the partial financial support from the American University of Sharjah through the Office of Research and Graduate Studies (FRG17-T-19).

References

- [1] Z.P. Lu, H. Wang, M.W. Chen, I. Baker, J.W. Yeh, C.T. Liu, T.G. Nieh, An assessment on the future development of high-entropy alloys: summary from a recent workshop, *Intermetallics* 66 (2015) 67–76.
- [2] D.B. Miracle, O.N. Senkov, A critical review of high entropy alloys and related concepts, *Acta Mater.* 122 (2017) 448–511.
- [3] J.W. Yeh, Recent progress in high-entropy alloys, *Ann. Chim. Sci. Des. Mater.* 31 (2006) 633–648.
- [4] Y. Zhang, T.T. Zuo, Z. Tang, M.C. Gao, K.A. Dahmen, P.K. Liaw, Z.P. Lu, Microstructures and properties of high-entropy alloys, *Progr. Mater. Sci.* 61 (2014) 1–93.
- [5] B. Cantor, I.T.H. Chang, P. Knight, A.J.B. Vincent, Microstructural development in equiatomic multicomponent alloys, *Mater. Sci. Eng.: A* 375–377 (2004) 213–218.
- [6] H.-P. Chou, Y.-S. Chang, S.-K. Chen, J.-W. Yeh, Microstructure, thermophysical and electrical properties in $\text{Al}_x\text{CoCrFeNi}$ ($0 \leq x \leq 2$) high-entropy alloys, *Mater. Sci. Eng.: B* 163 (2009) 184–189.
- [7] Z. Li, K.G. Pradeep, Y. Deng, D. Raabe, C.C. Tasan, Metastable high-entropy dual-phase alloys overcome the strength–ductility trade-off, *Nature* 534 (2016) 227.
- [8] D. Li, Y. Zhang, The ultrahigh charpy impact toughness of forged $\text{Al}_x\text{CoCrFeNi}$ high entropy alloys at room and cryogenic temperatures, *Intermetallics* 70 (2016) 24–28.
- [9] J. Joseph, N. Stanford, P. Hodgson, D.M. Fabijanic, Understanding the mechanical behaviour and the large strength/ductility differences between FCC and BCC $\text{Al}_x\text{CoCrFeNi}$ high entropy alloys, *J. Alloy. Compd.* 726 (2017) 885–895.
- [10] Z. Tang, O.N. Senkov, C.M. Parish, C. Zhang, F. Zhang, L.J. Santodonato, G. Wang, G. Zhao, F. Yang, P.K. Liaw, Tensile ductility of an AlCoCrFeNi multi-phase high-entropy alloy through hot isostatic pressing (HIP) and homogenization, *Mater. Sci. Eng.: A* 647 (2015) 229–240.
- [11] W.-R. Wang, W.-L. Wang, J.-W. Yeh, Phases, microstructure and mechanical properties of $\text{Al}_x\text{CoCrFeNi}$ high-entropy alloys at elevated temperatures, *J. Alloy. Compd.* 589 (2014) 143–152.
- [12] G.J. Shiflet, Low energy dislocation structures caused by phase transformation, *Mater. Sci. Eng.* 81 (1986) 61–100.
- [13] B. Gwalani, V. Soni, M. Lee, S.A. Mantri, Y. Ren, R. Banerjee, Optimizing the coupled effects of Hall-Petch and precipitation strengthening in a $\text{Al}_{0.3}\text{CoCrFeNi}$ high entropy alloy, *Mater. Des.* 121 (2017) 254–260.
- [14] A. Manzoni, H. Daoud, R. Völkl, U. Glatzel, N. Wanderka, Phase separation in equiatomic AlCoCrFeNi high-entropy alloy, *Ultramicroscopy* 132 (2013) 212–215.
- [15] M. Ogura, T. Fukushima, R. Zeller, P.H. Dederichs, Structure of the high-entropy alloy $\text{Al}_x\text{CrFeCoNi}$: fcc versus bcc, *J. Alloy. Compd.* 715 (2017) 454–459.
- [16] Y. Lu, Y. Dong, S. Guo, L. Jiang, H. Kang, T. Wang, B. Wen, Z. Wang, J. Jie, Z. Cao, H. Ruan, T. Li, A promising new class of high-temperature alloys: eutectic high-entropy alloys, *Sci. Rep.* 4 (2014) 6200.
- [17] T. Cao, J. Shang, J. Zhao, C. Cheng, R. Wang, H. Wang, The influence of Al elements on the structure and the creep behavior of $\text{Al}_x\text{CoCrFeNi}$ high entropy alloys, *Mater. Lett.* 164 (2016) 344–347.
- [18] T. Yang, S. Xia, S. Liu, C. Wang, S. Liu, Y. Zhang, J. Xue, S. Yan, Y. Wang, Effects of Al addition on microstructure and mechanical properties of $\text{Al}_x\text{CoCrFeNi}$ High-entropy alloy, *Mater. Sci. Eng.: A* 648 (2015) 15–22.
- [19] C. Zhang, F. Zhang, H. Diao, M.C. Gao, Z. Tang, J.D. Poplawsky, P.K. Liaw, Understanding phase stability of Al-Co-Cr-Fe-Ni high entropy alloys, *Mater. Des.* 109 (2016) 425–433.
- [20] Y.P. Wang, B.S. Li, M.X. Ren, C. Yang, H.Z. Fu, Microstructure and compressive properties of AlCrFeCoNi high entropy alloy, *Mater. Sci. Eng.: A* 491 (2008) 154–158.
- [21] T. Bhattacharjee, R. Zheng, Y. Chong, S. Sheikh, S. Guo, I.T. Clark, T. Okawa, I.S. Wani, P.P. Bhattacharjee, A. Shibata, N. Tsuji, Effect of low temperature on tensile properties of $\text{AlCoCrFeNi}_{2.1}$ eutectic high entropy alloy, *Mater. Chem. Phys.* (2017).
- [22] Z. Wu, H. Bei, G.M. Pharr, E.P. George, Temperature dependence of the mechanical properties of equiatomic solid solution alloys with face-centered cubic crystal structures, *Acta Mater.* 81 (2014) 428–441.
- [23] J. Joseph, T. Jarvis, X. Wu, N. Stanford, P. Hodgson, D.M. Fabijanic, Comparative study of the microstructures and mechanical properties of direct laser fabricated and arc-melted $\text{Al}_x\text{CoCrFeNi}$ high entropy alloys, *Mater. Sci. Eng.: A* 633 (2015) 184–193.
- [24] Y.-F. Kao, T.-J. Chen, S.-K. Chen, J.-W. Yeh, Microstructure and mechanical property of as-cast, -homogenized, and -deformed $\text{Al}_x\text{CoCrFeNi}$ ($0 \leq x \leq 2$) high-entropy alloys, *J. Alloy. Compd.* 488 (2009) 57–64.
- [25] K.S. Lee, B. Bae, J.H. Kang, K.R. Lim, Y.S. Na, Multi-phase refining of an AlCoCrFeNi high entropy alloy by hot compression, *Mater. Lett.* 198 (2017) 81–84.
- [26] Y. Lv, R. Hu, Z. Yao, J. Chen, D. Xu, Y. Liu, X. Fan, Cooling rate effect on microstructure and mechanical properties of $\text{Al}_x\text{CoCrFeNi}$ high entropy alloys, *Mater. Des.* 132 (2017) 392–399.
- [27] C.-M. Lin, H.-L. Tsai, Evolution of microstructure, hardness, and corrosion properties of high-entropy $\text{Al}_{0.5}\text{CoCrFeNi}$ alloy, *Intermetallics* 19 (2011) 288–294.
- [28] A. Munitz, S. Salhov, S. Hayun, N. Frage, Heat treatment impacts the micro-structure and mechanical properties of AlCoCrFeNi high entropy alloy, *J. Alloy. Compd.* 683 (2016) 221–230.
- [29] L. Ma, L. Wang, Z. Nie, F. Wang, Y. Xue, J. Zhou, T. Cao, Y. Wang, Y. Ren, Reversible deformation-induced martensitic transformation in $\text{Al}_{0.6}\text{CoCrFeNi}$ high-entropy alloy investigated by in situ synchrotron-based high-energy X-ray diffraction, *Acta Mater.* 128 (2017) 12–21.
- [30] I. Kireeva, Y. Chumlyakov, Z. Pobedennaya, A. Vyrodova, Temperature dependence of mechanical properties in [111]-oriented single crystals of $\text{CoCrFeNiAl}_{0.3}$ high

- entropy alloy, AIP Conf. Proc. 1909 (2017) 020083.
- [31] A. Gali, E.P. George, Tensile properties of high- and medium-entropy alloys, *Intermetallics* 39 (2013) 74–78.
- [32] Y. Deng, C.C. Tasan, K.G. Pradeep, H. Springer, A. Kostka, D. Raabe, Design of a twinning-induced plasticity high entropy alloy, *Acta Mater.* 94 (2015) 124–133.
- [33] Z. Zhang, M.M. Mao, J. Wang, B. Gludovatz, Z. Zhang, S.X. Mao, E.P. George, Q. Yu, R.O. Ritchie, Nanoscale origins of the damage tolerance of the high-entropy alloy CrMnFeCoNi, *Nat. Commun.* 6 (2015) 10143.
- [34] W.Z. Abuzaid, H. Sehitoglu, J. Lambros, Localisation of plastic strain at the microstructural level in Hastelloy X subjected to monotonic, fatigue, and creep loading: the role of grain boundaries and slip transmission, *Mater. High Temp.* 33 (2016) 384–400.
- [35] W. Abuzaid, H. Sehitoglu, Critical resolved shear stress for slip and twin nucleation in single crystalline FeNiCoCrMn high entropy alloy, *Mater. Charact.* 129 (2017) 288–299.
- [36] L. Patriarca, A. Ojha, H. Sehitoglu, Y.I. Chumlyakov, Slip nucleation in single crystal FeNiCoCrMn high entropy alloy, *Scr. Mater.* 112 (2016) 54–57.
- [37] L. Patriarca, W. Abuzaid, H. Sehitoglu, H.J. Maier, Y. Chumlyakov, Twin nucleation and migration in FeCr single crystals, *Mater. Charact.* 75 (2013) 165–175.
- [38] W. Abuzaid, H. Sehitoglu, J. Lambros, Plastic strain localization and fatigue microcrack formation in Hastelloy X, *Mater. Sci. Eng.: A* 561 (2013) 507–519.
- [39] J. Carroll, W. Abuzaid, J. Lambros, H. Sehitoglu, An experimental methodology to relate local strain to microstructural texture, *Rev. Sci. Instrum.* 81 (2010) 083703.
- [40] A.M. Sarosiek, W.S. Owen, The work hardening of dual-phase steels at small plastic strains, *Mater. Sci. Eng.* 66 (1984) 13–34.
- [41] L. Sun, R.H. Wagoner, Complex unloading behavior: nature of the deformation and its consistent constitutive representation, *Int. J. Plast.* 27 (2011) 1126–1144.
- [42] H. Ghassemi-Armaki, R. Maaß, S.P. Bhat, S. Sriram, J.R. Greer, K.S. Kumar, Deformation response of ferrite and martensite in a dual-phase steel, *Acta Mater.* 62 (2014) 197–211.
- [43] A. Govik, R. Rentmeester, L. Nilsson, A study of the unloading behaviour of dual phase steel, *Mater. Sci. Eng.: A* 602 (2014) 119–126.
- [44] X. Xue, J. Liao, G. Vincze, A.B. Pereira, F. Barlat, Experimental assessment of nonlinear elastic behaviour of dual-phase steels and application to springback prediction, *Int. J. Mech. Sci.* 117 (2016) 1–15.
- [45] S. Zarei, R.J. Nedoushan, M. Atapour, The sources of the micro stress and strain inhomogeneity in dual phase steels, *Mater. Sci. Eng.: A* 674 (2016) 384–396.